POLITECNICO DI TORINO
Repository ISTITUZIONALE

Multistage and passive cooling process driven by salinity difference

Original
Multistage and passive cooling process driven by salinity difference / Alberghini, M., Morciano, M., Fasano, M., Bertiglia, F., Fernicola, V., Asinari, P., Chiavazzo, E.. - In: SCIENCE ADVANCES. - ISSN 2375-2548. - ELETTRONICO. - 6:11(2020), p. eaax5015. [10.1126/sciadv.aax5015]

Availability:
This version is available at: 11583/2803232 since: 2020-04-18T17:38:11Z

Publisher:
AAAS - American Association for the Advancement of Science

Published
DOI:10.1126/sciadv.aax5015

Terms of use:

This article is made available under terms and conditions as specified in the corresponding bibliographic description in the repository

Publisher copyright

(Article begins on next page)

09 November 2026

APPLIED SCIENCES AND ENGINEERING

Multistage and passive cooling process driven by salinity difference

Matteo Alberghini[1,2]*, Matteo Morciano[1,2]*, Matteo Fasano[1], Fabio Bertiglia[3], Vito Fernicola[3], Pietro Asinari[1†], Eliodoro Chiavazzo[1†]

Copyright © 2020 The Authors, some rights reserved; exclusive licensee American Association for the Advancement of Science. No claim to original U.S. Government Works. Distributed under a Creative Commons Attribution NonCommercial License 4.0 (CC BY-NC).

Space cooling in buildings is anticipated to rise because of an increasing thermal comfort demand worldwide, and this calls for cost-effective and sustainable cooling technologies. We present a proof-of-concept multistage device, where a net cooling capacity and a temperature difference are demonstrated as long as two water solutions at disparate salinity are maintained. Each stage is made of two hydrophilic layers separated by a hydrophobic membrane. An imbalance in water activity in the two layers naturally causes a non-isothermal vapor flux across the membrane without requiring any mechanical ancillaries. One prototype of the device developed a specific cooling capacity of up to 170 W m^{-2} at a vanishing temperature difference, considering a 3.1 mol/kg calcium chloride solution. To provide perspective, if successfully up-scaled, this concept may help satisfy at least partially the cooling needs in hot, humid regions with naturally available salinity gradients.

INTRODUCTION

Cooling buildings or other facilities is a ubiquitous need in different climate areas. In Europe, 79% of the total final energy consumed in the households is required for heating and cooling purposes (*1*). While space cooling alone currently represents only a rather small share of energy consumption, recent studies suggest a rapidly increasing growth in part because of warmer summers due to climate change (*2*, *3*). Although cooling is often associated with thermal comfort, there is evidence that heat waves can cause about a thousand deaths per year even in developed countries (*4*).

Nowadays, vapor compression technologies are used for fulfilling most of the cooling demand despite their consuming substantial electricity and their possibility of causing seasonal peaks in the energy consumption. As an example, air conditioning is responsible for almost 16% of the total primary energy needed in buildings in the United States (*5*). In addition, vapor compression technologies typically involve refrigerants with high global warming potential (*6*). In recent years, several evaporative cooling technologies have been developed, representing a viable alternative to traditional air conditioning systems. Particularly, the Maisotsenko cycle (*7*) allows the cooling of inlet air from ambient conditions to the dew point temperature, exhibiting efficiencies from 1.5 to 4 times higher than traditional cooling systems based on vapor compression (*8*). However, the cooling potential of evaporative solutions strongly depends on the inlet conditions of ambient air, thus presenting substantial limitations when used in humid climates.

Environmentally friendly and possibly scalable approaches that provide a net cooling capacity without resorting to electricity may therefore be highly beneficial to reduce the energy consumption and alleviate the environmental impact of current cooling technologies. In this respect, daytime radiative cooling has recently shown an impressive level of development, as evidenced by the several published works (*9*–*15*). Radiative cooling is a passive approach because it self-operates without mechanical moving parts or auxiliary equipment. Although it is a rather old concept (*16*, *17*), only recent advances in material science have allowed substantial cooling capacity under daytime conditions, leading to highly scalable optical metamaterials with noontime radiative cooling power exceeding 90 W m^{-2} at a vanishing temperature difference (*11*, *12*). In addition to the intrinsic thermodynamic limitations of these systems [approximately 160 W m^{-2} (*13*)], this approach is inefficient in tropical regions with high humidity—where cooling is most often requested—because the possibility of radiating infrared radiation into the outer space is particularly challenging. Therefore, alternative passive cooling techniques that can be effective in high humidity or dusty conditions are highly desirable.

In this work, inspired by the work of Woods *et al.* (*18*), we design, realize, and experimentally test a passive cooling device. Unlike the device developed by Woods *et al.*, which presents an active absorption heat pump, our system operates without moving mechanical parts or auxiliary equipment and is thus referred to as a passive cooler henceforth. We would like to note, however, that the presented systems can be referred to as passive up to a certain boundary within which the device itself is embedded. Hence, pumps will be typically needed only to extract the cooling load from the evaporator and transfer it to the user by a fluid. Similarly, a fan for heat removal from the condenser would be beneficial for improving performance (although not necessary when relying upon natural convection). This feature is shared with other passive cooling devices from the literature [see, e.g., (*14*)].

Here, we would like to point out that the underlying idea of this work consists in demonstrating the development of a net cooling load at a nearly ambient pressure of a passive cooling technology based only on commonly available materials. The cooling load is generated by a salinity disparity between two aqueous solutions (here represented by distilled water and brine). Those solutions, kept separated by a hydrophobic microporous membrane, can only exchange water vapor. Under proper conditions, the difference in water activity generates a net vapor flux from the distilled water (evaporator) toward the brine (condenser). In particular, the evaporator

[1]Department of Energy "Galileo Ferraris", Politecnico di Torino, Corso Duca degli Abruzzi 24, Torino 10129, Italy. [2]Clean Water Center, Politecnico di Torino, Corso Duca degli Abruzzi 24, Torino 10129, Italy. [3]Applied Metrology and Engineering Division, INRIM Istituto Nazionale di Ricerca Metrologica, Strada delle Cacce 91, Torino 10135, Italy.
*These authors contributed equally to this work.
†Corresponding author. Email: eliodoro.chiavazzo@polito.it (E.C.); pietro.asinari@polito.it (P.A.)

Downloaded from http://advances.sciencemag.org/ on March 14, 2020

is made of a hydrophilic porous material connected to a distilled water reservoir, thus allowing a constant supply of distilled water by capillary action without the need of an active pump. The brine, however, is held in a cavity connected to a high-salinity reservoir. The above describes only one core unit of the tested device. Several units may be stacked so that the heat flux received by the lowest condenser is transferred to the second lowest evaporator, thus recovering the enthalpy of condensation. This multistage configuration allows an increase in the maximum temperature difference and cooling capacity achievable by a single-stage device. We found that our laboratory-scale prototype provides a maximum cooling capacity of nearly 100 W m^{-2} when it operates with a sodium chloride solution at 3.1 mol/kg and a maximum cooling capacity of approximately 170 W m^{-2} with a calcium chloride solution at the same concentration (extrapolated values at a vanishing temperature difference). A lumped parameter model is used to interpret the experimental results and to estimate the performance of the device under different operating conditions (e.g., different ambient temperatures, a different number of stages, or the presence of an air gap above the membrane), thus allowing the optimization of the device design to match specific working conditions. In essence, the present cooling device can be thought of as the opposite of the passive distiller recently proposed by some of the authors of this article (*19*).

We stress that the main value of this work consists in the scientific feasibility of the basic concept described above, with no claims on practical applicability under any real working conditions or at any industrially relevant scales. However, it is useful to report theoretical applications of the presented device. Thus, we believe that this concept can be exploited in hot or tropical regions where salt is naturally available, such as in the proximity of solar salt works or salt mines (*20*). Moreover, although beyond the main scope of this study, we also envision and theoretically investigate a possible cyclical process where the suggested device is coupled with a passive solar distillation system (*19*). In this sense, the proposed device can be considered a first step toward fully passive solar cooling cycles, where solar energy is used to drive the distillation device to generate two solutions at different salinities, which can be either stored or readily used for cooling. Unlike passive radiative cooling technologies, in the suggested system, solar energy should sustain the cooling process instead of being reflected. One possible advantage of our proposed cooling system is that it can intrinsically store the cooling capacity in a potential form (i.e., salinity difference), therefore being able to adjust for different availabilities of solar energy based on time and variable cooling demands.

RESULTS

Passive cooling principle and implementation

The proposed device provides a cooling capacity by exploiting the salinity difference between two solutions (see the schematic in Fig. 1A). The salinity disparity causes a vapor pressure difference between the solutions resulting in a net vapor flux from the evaporating layer to the condensing layer and in a net cooling load in this single-stage device. Multistage configurations are possible by using the enthalpy of condensation of one stage to drive the solvent evaporation in the subsequent one. These evaporation-condensation processes remove heat from the lower-temperature chamber (T_F) and transfer it into the higher temperature (T_A) external ambient. The device is able to operate without any moving mechanical parts or auxiliary equipment, and, in this sense, it is classified as a passive cooling technology.

Our tested laboratory-scale prototype of the passive cooler consists of four identical stages, where in each stage a hydrophobic microporous membrane keeps two liquid phases separated by a submillimeter distance (see Fig. 1B). One liquid phase with high salinity is contained in a thin cavity at the top part of each stage and consists of a salt (e.g., sodium chloride) solution at fixed salinity. The second liquid phase with low salinity is embedded in a thin hydrophilic layer at the bottom part of the stage. In our setup, the latter liquid phase consists of distilled water. Each stage is sandwiched by two thin aluminum plates, which separate successive stages while easing conductive heat transfer through the device. A thin hydrophilic strip is connected to the hydrophilic layer located at the bottom of each stage and ensures a continuous supply of distilled water from a storage basin by capillary forces alone, without the need of a pump or any other circulation means. The salt water basin, instead, is positioned to induce a small hydraulic head (≈15 cm) in the condensers, thus ensuring their complete filling during operations. In general, heat sinks should be attached to the top and bottom sides of the cooler to enhance heat transfer with the external environment and the refrigerated chamber, respectively.

A single stage of the cooler is detailed in Fig. 1C along with the characteristic driving forces of the process. The difference in salinity, and thus water activity, causes a vapor pressure disparity between the two liquid phases, which is, in turn, responsible for a net water vapor flux from the distilled water (i.e., the evaporator) to salt solution (i.e., the condenser). A transfer of enthalpy of evaporation occurs in this process, and this establishes a temperature difference across the membrane: Salt water in the cavity is heated, while distilled water in the hydrophilic layer is cooled. Such a temperature gradient across the membrane is opposed to the activity gradient, thus reducing the net vapor flux. As a result, the actual working condition of each stage of the cooler comes from a balance between the contrasting temperature and activity effects on the overall vapor pressure across the membrane (see Materials and Methods for a detailed discussion on this aspect).

The main components of our specific prototype of one cooling stage are shown in Fig. 1D. Each stage is implemented in a three-dimensional (3D)–printed plastic frame, which is made of acrylonitrile butadiene styrene (Dimension Elite, Stratasys supplied by TM Technimold srl, Genova, Italy) treated with a polymeric sealer (Nano-Seal 180W, supplied by JELN Imprägnierung GmbH, Schwalmtal, Germany). The hydrophobic membrane is made of polytetrafluoroethylene (1.0-μm pores, ANOW Microfiltration supplied by Hangzhou Anow Microfiltration Co. Ltd., Hangzhou City, China; see note S1 for a detailed characterization) and is glued to the bottom of the plastic frame. The top of the plastic frame, instead, has a 2-mm cavity containing salt water, which is enclosed by an aluminum plate cover (thickness, 1 mm). The hydrophilic layer saturated by distilled water and positioned below the membrane is made of microfiber, and it is supported by an aluminum plate (thickness, 1 mm) at the bottom. The cooling prototype has an effective thermal area of $A_{net} = 1.69 \times 10^{-2}$ m^2. Our cooling device is highly modular and flexible; depending on the target cooling capacity, a variable number of stages can be easily assembled, and different salt solutions can be adopted (below the saturation limit, at operating temperature).

Downloaded from http://advances.sciencemag.org/ on March 14, 2020

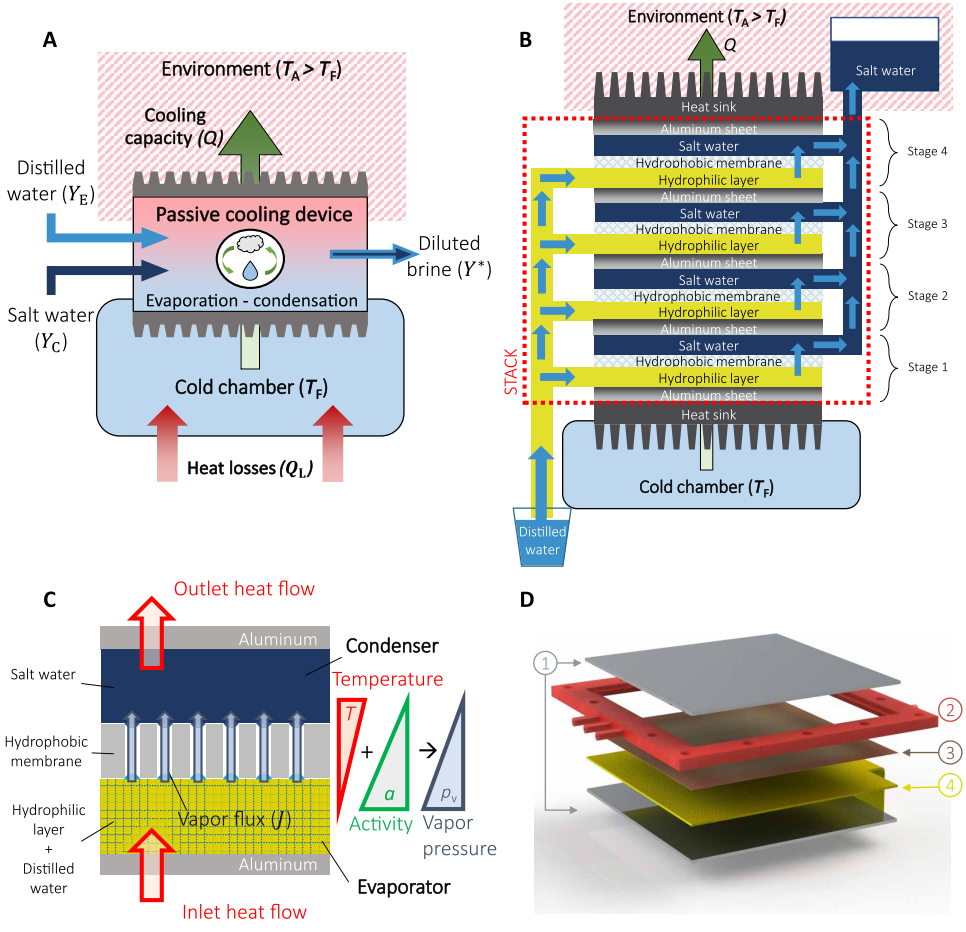

Fig. 1. Layout, schematics, and working principle of the passive cooling device. (**A**) Schematic of the working principle of a generic salinity-driven cooler: The salinity difference between two inlet solutions generates a net vapor flux from the evaporating (Y_E) to the condensing (Y_C) layers. These evaporation-condensation processes in multiple stages allow the removal of heat from the lower-temperature chamber and the transfer of heat into the higher-temperature external environment. This process eventually leads to a by-product, being the dilution of the solution in the condensers, which is here represented as an outlet flow with an intermediate salinity (Y^*) with respect to the inlet solution at Y_C. (**B**) Schematic layout of the four-stage modular passive cooler discussed in this work. The actual experimental setup is reported in fig. S1. (**C**) Working principle of one stage of the passive cooler: Two solutions with different salinities are separated from each other by a hydrophobic membrane. The salt concentration difference creates an activity gradient (green triangle), which leads to a net vapor flux. The transfer of enthalpy of evaporation establishes a temperature gradient between the two solutions (red triangle), which is opposed to the gradient created by the activity difference. (**D**) Graphical representation of the assembly of one stage of the cooling device. A 3D-printed plastic frame (2, red) contains the cavity that forms the condenser, which is sealed by an aluminum plate cover (1, gray) and a hydrophobic membrane (3, brown). The hydrophilic layer (4, yellow), being the evaporator, is placed between the membrane and another aluminum plate.

Cooling performance

The cooling performance of a four-stage prototype was assessed with the test rig in fig. S1A, considering the constant ambient temperature [$T_A = (30.0 \pm 0.5)$°C] and salinity of the NaCl-water solution [$Y_C = (170 \pm 2)$ g/liter]. Thirteen independent tests were carried out to obtain the characteristic $q - \Delta T$ curve of the cooler, where q is the specific cooling capacity (i.e., cooling capacity normalized by A_{net}) and ΔT is the temperature difference between the first-stage evaporator and last-stage condenser. During the experiments, a heat sink was placed between the last-stage condenser and the external ambient, whereas all the other sides of the prototype were covered by insulating material to reduce thermal loss. In each test, the prototype was subjected to a specific thermal load (q) supplied by two silicon heaters positioned below the first-stage evaporator (see figs. S1B and S2), thus leading to a steady-state temperature difference through the cooler (ΔT). The minimum cooling capacity was achieved when the electrical heaters were switched off, and the thermal power removed by the cooler only accounted for thermal losses. Thus, the maximum ΔT could be observed. When heaters were switched on, the cooling capacity increased and thus ΔT was reduced. Details on the experimental setup and protocol are provided in Materials and Methods, and an extended discussion on the uncertainty analysis of measurements is reported in note S2.

Figure 2A presents the typical time evolution of the temperature of the external environment (green line), first-stage evaporator (blue line), and last-stage condenser (red line) of the prototype, during a test with $q \approx 25$ W m^{-2} applied thermal load. When the cooler starts to operate ($t = 0$ s), the condenser temperature rapidly increases above the ambient temperature, thus causing a net heat flux from the condenser to the surrounding environment. At the same time, the evaporator temperature decreases below the ambient temperature, thus providing a cooling effect. In the tests, we considered the cooler under steady-state conditions when each measured temperature shows variations lower than 3×10^{-4} K s^{-1} over 150 samples

Downloaded from http://advances.sciencemag.org/ on March 14, 2020

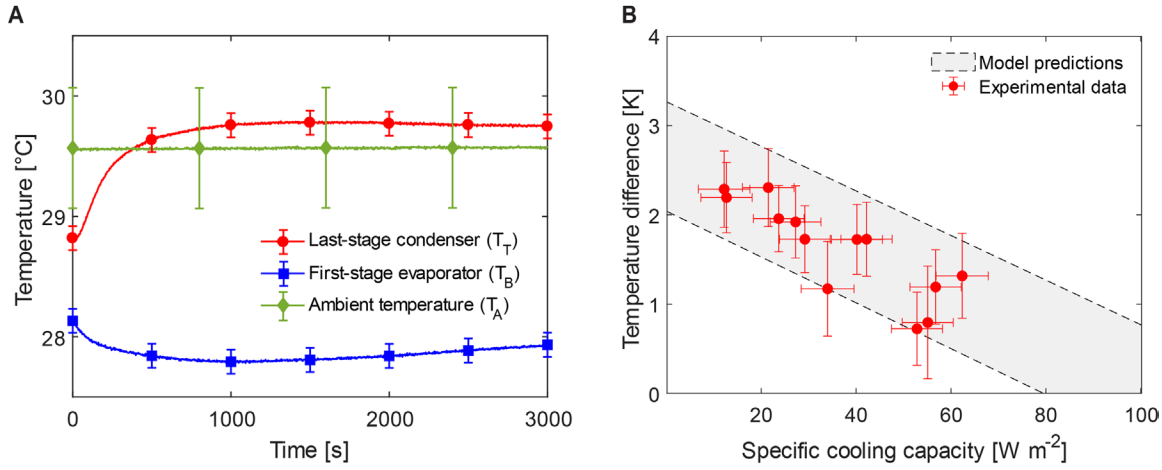

Fig. 2. Experimental cooling performance. (**A**) Time evolution of the last-stage condenser (red), first-stage evaporator (blue), and ambient (green) temperatures during a typical laboratory test with the 3.1 mol/kg NaCl solution (25 W m^{-2} thermal load). (**B**) Experimental results (red dots) and modeling predictions (gray band) of the specific cooling capacity of the passive cooler with respect to the considered temperature difference across the device with the 3.1 mol/kg NaCl solution. See note S2 for details on the reported error bars of the experiments. Modeling predictions are obtained with Eqs. 3 to 24, and the reported band is enclosed between the minimum and maximum values obtained by varying the main input parameters of the model according to their bounds, namely, the activity, membrane thickness, and porosity (see table S1 for details).

(samples are recorded every 1 s), with the steady state being generally reached after 10 min of operation. The operating ΔT achieved for a specific q is then evaluated by computing the average temperature difference between the first-stage evaporator and last-stage condenser, considering a 1500-s time interval of measures at the steady state. Because the experiments were performed in batches, namely, with a fixed amount of distilled and salt water in the respective feeding basins, the vapor flux from the evaporators progressively diluted the salt solution in the condensers, gradually reducing the difference in chemical potential across the membrane. As noticeable in Fig. 2A, this leads to a progressive reduction in the cooling performance of the cooler, specifically as it relates to decreasing ΔT with time. Stable operation of the passive cooler for longer times could be eventually achieved by continuously regenerating the salinity level in the condenser layers. A detailed discussion on this aspect is reported in note S3 and fig. S3.

The device was tested in a controlled temperature chamber. Two silicone heaters are used to provide the specific thermal loads. A forced convection heat sink is used to improve the heat transfer between the last-stage condenser (i.e., the aluminum cover on the top of the cooler) and the environment. The temperature drop across the device is measured by means of four 100-ohm platinum resistance thermometers (PRTs). The full description of the experimental setup and testing protocol can be found in Materials and Methods. The obtained $q - \Delta T$ characteristic curve of the prototype is reported in Fig. 2B, where experimental data are represented as red circles. The maximum cooling capacity achieved by the prototype—corresponding to a vanishing temperature difference across it—is extrapolated by a linear interpolation of the experimental results and is approximately equal to 100 W m^{-2}. From this condition, a progressive increase in ΔT causes a reduction in q because a greater part of the enthalpy of evaporation from evaporators to condensers is devoted to contrast the sensible heat flux across the device. At the limit, when the thermal power removed by the cooler is null, the evaporation-condensation process only sustains the maximum achievable ΔT, which is approximately 3 K. The average consumption of distilled water in the evaporators increases with q, with values ranging from 2.3 to 3.0 liters m^{-2} hour^{-1} (see fig. S4A). Notice that, for the entire duration of the tests (2 months), no fouling or scaling was observed on the selected membranes or hydrophilic layers and, therefore, no notable degradation of cooling performance was noticed for the tested prototype over time. The raw data of these experiments are fully available in dataset S1.

The experimental results are then interpreted with the lumped parameter model described in Materials and Methods, whose predictions are reported as a gray band in Fig. 2B. Modeling predictions display a reasonably good agreement with the experimental measures, at least within the uncertainty interval of the model (gray band). The model uncertainty is estimated considering the highest and lowest predictions obtained within the explored interval of the model parameters: Boundary values are assigned to the parameters that mainly affect the vapor transport across the membrane according to their uncertainty, and their combinations are explored (see table S1 for details). The value of the membrane permeability estimated by the model is equal to $(6.8 \pm 1.5) \times 10^{-7}$ kg m^{-2} Pa^{-1} s^{-1}, which is in good agreement with the experimental value of $(6.8 \pm 1.1) \times 10^{-7}$ kg m^{-2} Pa^{-1} s^{-1} (see fig. S5).

Cooling performance under different operating conditions

The cooling performance of the passive cooler depends on the considered operating conditions and design parameters, for instance, on the selected salt solution, number of assembled stages, external ambient temperature, and stratigraphy of each cooling stage. The water activity in the salt solution in the condensers is a main parameter that affects the transfer of enthalpy of evaporation across the membrane and, hence, the cooling capacity. The water activity depends on the type and molality of dissolved salt ions. First, the performance of the four-stage prototype is experimentally assessed when operating with an aqueous $CaCl_2$ solution at the same molal concentration (3.1 mol/kg) and ambient temperature (T_A = 30°C) of the NaCl solution used in the previous experiments. The tests are performed by applying the same experimental protocol described previously. Because of a more pronounced reduction in the water activity, the $q - \Delta T$ characteristic curve shows a notable increase

Downloaded from http://advances.sciencemag.org/ on March 14, 2020

in the maximum temperature difference and specific cooling capacity obtainable from the passive cooler, which are enhanced up to approximately 4.5 K and 170 W m^{-2}, respectively. We note that the latter cooling capacity is the extrapolated value at the intersection of the experimental regression line and the horizontal axis in Fig. 3A, whereas the highest measured value is 110 W m^{-2} with a temperature difference of 2 K. The larger flux of enthalpy of evaporation also leads to a higher consumption of distilled water (3.5 to 4.5 liters m^{-2} $hour^{-1}$ depending on the cooling power; see fig. S4B) with respect to the cooling device operated with sodium chloride (see also the raw data of those experiments in dataset S2). The experimental results (black dots) are compared with the modeling predictions (yellow band) in Fig. 3A, showing good agreement. The upper and lower bounds of the main parameters of the model used to estimate its uncertainty band are reported in table S1. Second, the lumped parameter model—validated against the experimental results in Figs. 2B and 3A—is used to also explore the effect of molality on the characteristic $q - \Delta T$ curve of the passive cooler. For example, the molality of the NaCl solution is varied while still considering a four-stage cooler at T_A = 30°C. Starting from the value considered in the experiments (3.1 mol/kg), model predictions show a large decrease in the cooling performance with a lower molality. Considering a NaCl solution with a typical seawater salinity (0.6 mol/kg), the maximum temperature difference and specific cooling capacity drop to 0.6 K and 20 W m^{-2}, respectively.

The effect of the ambient temperature on the cooling capacity of the proposed device is also investigated by the model. Specifically, Fig. 3B shows the cooling performance as a function of environmental temperatures (T_A) ranging from 15 to 40°C. The results show better cooling performance at higher ambient temperatures owing to the enhanced evaporation process, as evidenced from the temperature dependence of Antoine's equation (see Eq. 4). Considering typical summer conditions (e.g., T_A = 40°C), the cooling capacity can reach values up to 165 W m^{-2} at a vanishing temperature difference.

In Fig. 3C, the lumped parameter model is used to estimate how the number of stacked modular stages (N) affects the cooling performance of the resulting multistage device. On the one hand, the

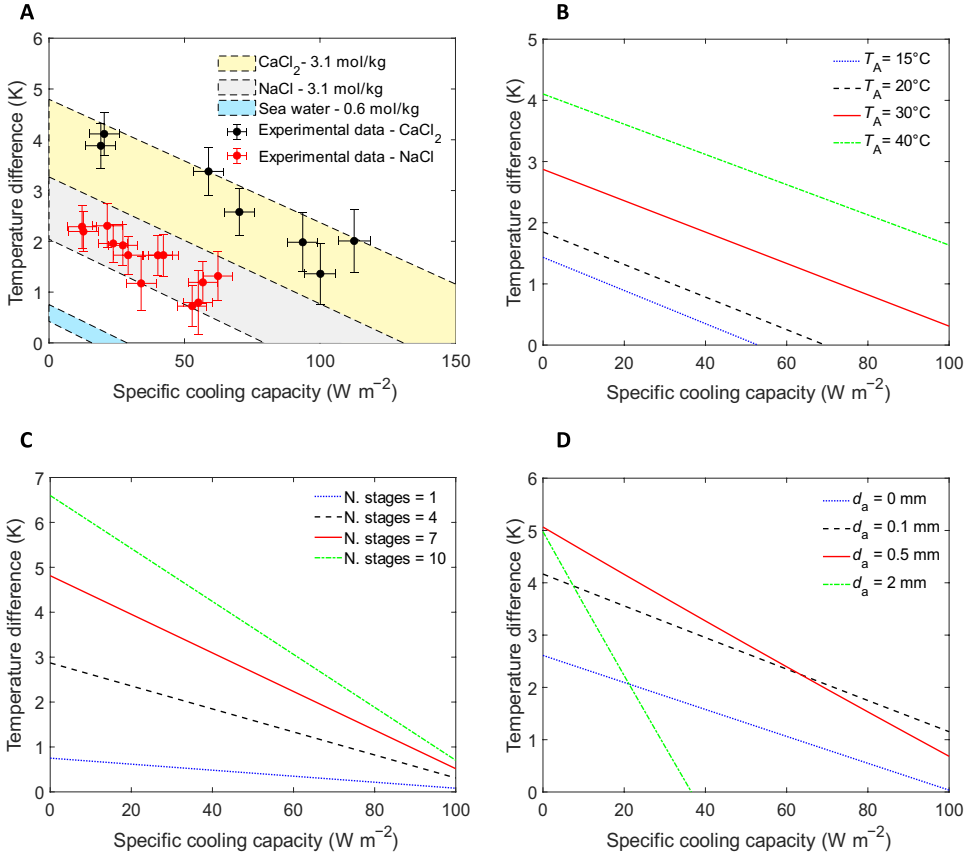

Fig. 3. Cooling performance with different configurations. (**A**) Cooling performance of the four-stage passive cooler as predicted by the lumped parameter model for different aqueous solutions. While the evaporators contain distilled water in all cases, the condensers are supposed to contain seawater (0.6 mol/kg, blue band), a 3.1 mol/kg solution of NaCl (gray band), or a 3.1 mol/kg solution of $CaCl_2$ (yellow band). (**B**) Modeling predictions for the four-stage passive cooler at different ambient temperatures (T_A) but a fixed 3.1 mol/kg NaCl solution. According to Eq. 4, a higher T_A implies greater vapor fluxes through the membrane, hence better cooling performance than the case that was experimentally assessed (solid red line, T_A = 30°C). The increase in cooling capacity with the ambient temperature is mainly due to the exponential increase of vapor pressure with temperature, as predicted by Antoine's law. (**C**) Modeling predictions for the passive cooler with different numbers of stages but a fixed 3.1 mol/kg NaCl solution and T_A = 30°C. Increasing the number of stages substantially increases the maximum temperature difference achievable across the device owing to the reduction of the temperature across each membrane. (**D**) Modeling predictions for the four-stage passive cooler considering an additional air gap beneath the membrane, as predicted by the lumped parameter model. In detail, the performance of the cooling device is estimated by varying the thickness of the additional air gap (d_a) from 0 to 2 mm, with a 3.1 mol/kg NaCl solution and T_A = 30°C. All the model parameters used in (A) to (D) are reported in table S1.

Downloaded from http://advances.sciencemag.org/ on March 14, 2020

maximum cooling capacity is only increased by ≈15% when moving from one to four stages. On the other hand, the maximum ΔT achievable with a 10-stage configuration is twice that obtained with the setup tested experimentally (four stages, black dashed line). Notice that the evaporation rate in the different stages is not uniform across the multistage device because of the different working temperatures of each stage. See also note S4 for an exergy analysis of these multistage configurations of the cooler.

In Fig. 3D, the inclusion of an air gap beneath the tested membrane was investigated by the model. This air gap could be practically kept by means of a porous spacer (see, e.g., fig. S6). We specifically focus on the above geometrical parameter because, in our experience, it is the one that mostly affects the cooling performance of the passive device. The thickness of the additional air gap (d_a) varies from 0 to 2 mm in the analysis. Model predictions show that air gap with a thickness of 100 μm leads to a temperature difference increase as high as 60% owing to the thermal resistance enhancement. Similarly, a 50% reduction in the distilled water consumption occurs because of the lower permeability (see fig. S7). However, an increased thickness of the air gap has beneficial effects on the performance up to a threshold value of d_a. Beyond this value, the increased temperature difference across each stage is not large enough to balance the negative effect from the permeability reduction. When d_a is larger than 0.5 mm, performance starts to deteriorate because of the reduced mass transfer permeability responsible for low evaporation. This effect is more pronounced at higher cooling capacities, where the temperature difference is lower and less effective at counteracting the reduction in permeability.

The experimental results obtained for the proposed passive cooler are finally compared with the performance of different passive cooling technologies found in the literature (see note S5). In particular, Fig. 4 highlights that the extrapolated maximum cooling capacity of the passive device observed in our experiments (four stages, $CaCl_2$ solution, 3.1 mol/kg, T_A = 30°C) is 50% higher with respect to the best-performing daytime radiative cooler from the literature, and it eventually exceeds the theoretical limit of radiative cooling without relying on favorable atmospheric conditions (*13*). It is worth pointing out that the present device is based on completely different physical phenomena compared with passive radiative systems, and they are reported here only for providing the reader with a reference. For the sake of fairness, we should also point out that the comparison is meaningful if the concentration difference between the salt solutions in the cooler is initially available. However, more care is needed when the concentration difference should be sustained by solar distillation because low-activity water solutions are associated not only with the highest cooling performance but also with the lowest distillation productivities.

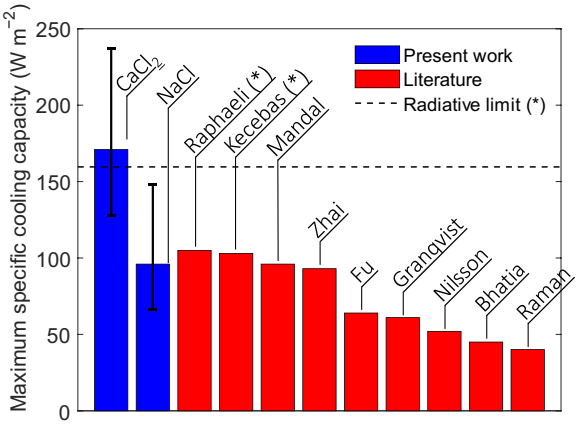

Fig. 4. Comparison with other passive cooling technologies. Comparison between the performance of the proposed device and different daytime radiative cooling technologies from the literature. The results reported refer to the works of Rephaeli *et al.* (*36*), Kecebas *et al.* (*37*), Mandal *et al.* (*12*), Zhai *et al.* (*11*), Fu *et al.* (*38*), Granqvist and Hjortsberg (*16*), Nilsson *et al.* (*39*), Bhatia *et al.* (*40*), and Raman *et al.* (*10*). The references labeled with an asterisk refer to modeling results. The maximum specific cooling capacity at a vanishing temperature difference for the proposed device and its uncertainties are estimated from the experimental results by linear fitting (least square method). The thermodynamic limit of daytime radiative cooling is computed at T_A = 30°C (*13*).

Passive solar cooling

A detailed characterization of the proposed passive cooler, under well-defined operating conditions, led to the characteristic curves reported in Figs. 2 and 3. Without a loss of generality, our experiments were conducted in batch conditions. Therefore, after a sufficient period, the salt solution in the condensers was progressively diluted by the water vapor flux through the membrane, thus resulting in a reduction in the cooling driving force over time. Technological applications of the present passive cooler alone can be envisioned mostly in hot regions with a natural availability of high-salinity solutions (e.g., near solar saltworks or salt mines). Moreover, alternative applications can also be imagined, if a continuous regeneration of the salinity difference between evaporators and condensers is ensured.

To this end, coupling the passive cooler with the passive solar distiller proposed by some of the authors of this article (*19*) or any other passive solar distillation device (*21*) (not experimentally done in this work) would possibly result in a passive and off-grid solar-driven cooling system in the future. Passive distillers exploit solar energy to separate fresh water from a feeding salt solution. Hence, the salinity of the solution in the inlet basin increases, whereas the produced distillate is discharged into the outlet basin, therefore counterbalancing the opposite action of the cooler. In this sense, the present passive cooler may represent a first step toward a fully passive solar cooling technology. A possible scheme of the coupled system and the related thermodynamic cycle is shown in Fig. 5A and fig. S8, whereas the effect of salt water activity on the regeneration of the diluted solution is analyzed in note S6 and fig. S9. Here, for the sake of simplicity, both the cooling and distillation devices are depicted as composed by a single stage. Notice that the distiller is imagined above the cooling device to favor good salt stratification into the salt water basin. In the representation, the working temperatures of the condensers and evaporators of both devices are supposed to be equal to those of the environment they are in contact with, namely, the ambient (T_A) and cold chamber (T_F) temperatures.

Assuming a constant solar irradiance driving the distillation process and equilibrium conditions, a steady salinity difference between the distilled (Y_E) and salt (Y_C) water basins should be eventually achieved in the coupled system. In particular, the outlet solution from the cooling device (point 1 in Fig. 5B, with Y_C concentration and T_A temperature) is heated by the solar absorber (point 2, with Y_C concentration and T_H temperature). Then, the temperature difference through the distiller triggers the evaporation-condensation process, thus generating distilled water (point 3, with Y_E concentration and T_A temperature), which can readily feed the cooler and provide

Downloaded from http://advances.sciencemag.org/ on March 14, 2020

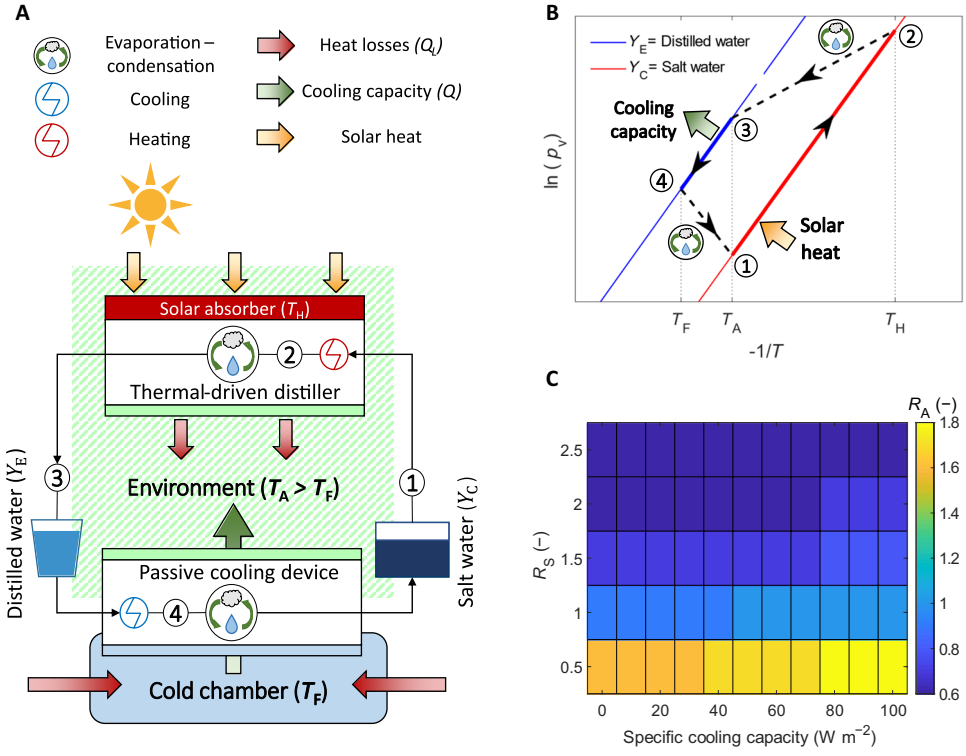

Fig. 5. Stable operating cycle of the passive cooler. (**A**) Schematic of a possible coupling between the passive cooler and a thermal-driven device for salt water distillation. In the latter device, an external source of heat (e.g., solar) allows water to be distilled from salt water, specifically to regenerate the salinity gradient between the two solutions. Therefore, if the distilled water equals that consumed by the cooler, a stable and passive cooling cycle can be established. The heat dissipation from the top condenser of the cooler and the bottom condenser of the distiller can be ensured by either natural or forced convection. (**B**) Representation in the Clapeyron chart of a possible coupling between the passive cooler and a thermal-driven device for salt water distillation. For simplicity, the temperatures of evaporators and condensers are equal to those of the surrounding environments (T_A and T_F, respectively). The salt water contained in the condenser operates ideally at ambient temperature (T_A) and constant concentration (Y_C) (point 1). The draw solution, diluted by the cooling device, is constantly regenerated by the solar distiller. A selective solar receiver passively heats the salt water (point 2, temperature T_H), producing distilled water (Y_E) at ambient temperature (point 3). This can be used by the proposed device (point 4) to cool a chamber to a temperature lower than the environmental temperature. (**C**) Coupling between the cooling device and the passive solar distiller proposed by some of the authors (*19*). R_S is the ratio between the number of stages of the distiller and those of the cooler; R_A is the ratio between the solar collecting area of the distiller and the active area of the cooler. Potential regeneration capabilities of the salinity gradient in the cooler are evaluated considering that the condensers are fed by salt water, with NaCl concentration equal to 170 g liter^{-1}.

the cooling effect to the refrigerated chamber (point 4, with Y_E concentration and T_F temperature) by means of the salinity-driven evaporation process.

Theoretical predictions of stable operating cycles for such a solar passive cooler are reported in Fig. 5C. By specifically referring to the distiller in (*19*), achieving continuous regeneration of the salinity difference is possible by properly selecting the number of stages and the solar absorbing area of the passive solar distiller. This should be done while considering the required specific cooling power. In the plot, $R_S = \frac{N_{Distiller}}{N_{Cooler}}$ is defined as the ratio between the number of stages of the distiller and those of the cooler, while $R_A = \frac{A_{Distiller}}{A_{Cooler}}$ is defined as the ratio between the solar collecting area of the distiller and the active area of the cooler. Therefore, according to the user needs, the two design parameters (R_S and R_A) can be varied to achieve a fully coupled distillation/cooling cycle while keeping the geometrical requirements of the specific application. For the sake of simplicity, N_{Cooler} is fixed to four to represent the experimentally tested configuration. The considered performance of the solar passive distiller is based on model predictions for an optimized configuration of the device in (*19*). Specifically, the interface between the evaporation and condensation layers includes both a 0.5-mm air gap and a hydrophobic membrane with a 3.0-μm pore size. Then, modeling estimates are evaluated considering an equivalent solar irradiance of 1 kW m^{-2}, ambient temperature (T_A) of 30°C, and a convective heat transfer coefficient equal to 5 W m^{-2} K^{-1}. As far as the performance of the passive cooling device is concerned, averaged values from table S1 are considered, specifically, a = 0.8994, d_m = 110 μm, and ϵ_m = 0.8. Note that to limit the temperature of the solar absorber, the maximum number of stages of distillation is 10; as a consequence, R_A ranges from 0.6 to 1.8 to achieve continuous regeneration. An estimation of the coefficient of performance for the solar cooling cycle made of the considered passive distiller and cooler coupled together is provided in note S7.

While Fig. 5B shows a generic ideal cycle for illustrative purposes, here, we provide additional details on the actual cycle for one specific coupled configuration with R_S = 1, R_A = 1, and the specific cooling power of 100 W m^{-2}. In that configuration, the cooling device consumes distilled water (≈2.85 liters m^{-2} hour^{-1}), while the productivity of the distiller is ≈2.95 liters m^{-2} hour^{-1} [according to estimates from the model and experiments reported in (*19*)]. This

Downloaded from http://advances.sciencemag.org/ on March 14, 2020

yields the cycle points reported in Table 1. Points 3 and 4 present the same thermodynamic conditions because of the vanishing temperature difference in case of the maximum extracted power.

The feasibility and performance of possible couplings between the passive cooler and some typical desalination technologies (namely, mechanical vapor compression, reverse osmosis, membrane distillation, and forward osmosis) are discussed in note S8.

DISCUSSION

In this study, we experimentally tested a modular and passive cooling process driven by the salinity difference in two aqueous solutions. The cooling process is established without resorting to fluid circulation means or any moving mechanical parts, and it only relies on capillarity and gravity (i.e., it is a passive device). Experimental tests were carried out on a four-stage laboratory-scale prototype operating in an ambient temperature of approximately 30°C, and the results were used to validate a 1D lumped parameter model of the cooling process. In the experiments, an aqueous NaCl solution at 3.1 mol/kg provided a maximum cooling capacity of approximately 60 W m^{-2} and an extrapolated value of nearly 100 W m^{-2} at a vanishing temperature difference. The adoption of an aqueous $CaCl_2$ solution at 3.1 mol/kg, instead, leads to a substantial increase in device performance, with a maximum cooling capacity of approximately 110 W m^{-2} and an extrapolated value of nearly 170 W m^{-2} at a vanishing temperature difference. The latter cooling capacity is notably above the performance of other passive daytime approaches to cooling, e.g., radiative coolers. The validated model was finally used to predict the performance of the passive cooler under a wider range of operating conditions.

As a future perspective beyond the main scope of this work, the passive cooler could be coupled with a solar distiller to sustain continuous operations because the distiller could provide both a steady flow of distilled water to the evaporators and keep a constant salinity in the salt water basin connected to the condensers. We stress that in our specific realization, microporous hydrophobic membranes were needed to separate the salt water in the cavity (condenser) from the distillate in the hydrophilic layer (evaporator). However, a membrane-free configuration can be envisioned if, in each stage, the condenser cavity is substituted with a hydrophilic layer containing salt water: In this way, a simple spacer should be used to keep the two hydrophilic layers (evaporator and condenser) separated at a fixed distance. Furthermore, a scaled-up implementation of the passive cooler should also optimize its cost and environmental impact (some discussions on these aspects can be found in notes S9 and S10, respectively).

Table 1. Cycle points for a complete solar cooling cycle. Actual Clapeyron cycle points referred to the case with $R_S = 1$, $R_A = 1$, and a specific cooling power of 100 W m^{-2} (see also Fig. 5).

	Y (g liter^{-1})	T (°C)	$-\frac{1}{T}$(K^{-1})	p_v(bar)	ln(p_v)
1	$Y_C = 170$	$T_A = 30.0$	-3.29×10^{-3}	3.74×10^{-3}	8.22
2	$Y_C = 170$	$T_H = 67.4$	-2.93×10^{-3}	24.52×10^{-3}	10.10
3	$Y_E = 0$	$T_A = 30.0$	-3.29×10^{-3}	4.15×10^{-3}	8.33
4	$Y_E = 0$	$T_F = 30.0$	-3.29×10^{-3}	4.15×10^{-3}	8.33

In principle, a closed cooling cycle made of the passive distiller and cooler could be implemented by means of a broad variety of solutions, including ones currently used in absorption refrigeration. However, for the moment, we have decided not to explore these possibilities because the typical absorption pairs used in those systems, e.g., water-ammonia or water–lithium bromide, may have a nonnegligible impact on the environment (*22*, *23*). Furthermore, corrosion and crystallization are other major disadvantages of using these solutions. Therefore, we have decided to focus our initial investigation on more sustainable solutions, namely, water–sodium chloride and water–calcium chloride solutions. Future studies could focus on estimating and assessing the performance of the passive cooler with different solutions to further enhance the specific cooling capacity of the device.

Note that, although the achievable temperature differences in passive cooling systems are in the order of a few kelvin, when those technologies are used for energy-saving purposes, they can potentially lead to important advantages, as, for instance, demonstrated by Raman *et al.* (*10*). Alternatively, following Goldstein *et al.* (*14*), substantial energy saving can be accomplished by combining passive cooling technologies with traditional vapor compression refrigeration systems because this coupling would allow the refrigerant to cool at sub-ambient temperatures. In this sense, the proposed passive cooler may help in implementing energy-saving strategies in future sustainable air conditioning and personal thermal management systems. The reader should finally observe that having a few kelvin degrees as a maximum possible temperature difference in the characteristic curves of Figs. 2 and 3 implies that, should the real boundary conditions impose a larger temperature gap between the two extreme surfaces, the device stops working. Such a condition might occur when there is intense solar radiation on the top surface of the device. How to possibly operate under those conditions is discussed in detail in note S11 and figs. S10 and S11.

MATERIALS AND METHODS

Experimental setup

To assess the performance of the cooling device, we implemented the test rig represented in fig. S1. The experimental setup includes a temperature-controlled test chamber, the prototype of the passive cooler, and two flat silicone heaters with their power supply. Four 100-ohm thin-film PRTs, a DC amperemeter, a precision scale, and a digital refractometer are used for measuring temperatures, heat flux, distillate mass, and the salinity of the aqueous solutions, respectively.

The passive cooler is tested in a chamber with controlled temperature (M120-VF oven, MPM Instruments), which mimics the external environment at a fixed T_A. The chamber temperature was set at 30°C during all the experiments. The accuracy of the set point reported on the data sheet of the chamber used during the experiments is ±1.5°C. However, the data collected during the current and other previous experimental campaigns allow an estimate at an uncertainty of the set-point temperature of ±0.5°C.

The cooler prototype is enclosed in a polystyrene box to minimize thermal loss toward the chamber. The last-stage condenser (i.e., the aluminum plate on the top surface of the cooler) is the only side of the cooler in direct contact with the surrounding ambient temperature during the tests. This side is glued (with a heat sink compound with a thermal conductivity of 0.65 W m^{-1} K^{-1}, RS Pro)

Downloaded from http://advances.sciencemag.org/ on March 14, 2020

to a heat sink operated under forced convection (with a heat sink convective resistance in the order of 1.7 K W^{-1}) to improve heat transfer with the controlled temperature chamber. Two flat silicone heaters (57.6 ohms; francoCorradi) powered by an electric power supply (PS 3003, HQ Power) are glued to the bottom aluminum plate of the cooler (i.e., first-stage evaporator) to provide a tunable heat flux (*24*). The hydrophilic strips connecting evaporators with the distilled water basin are covered by polyethylene film to minimize water evaporation in the environment. The cooler assembly is kept together by four M5 bolts placed at the corners of the plastic frames. Details on the durability and corrosion of the cooler prototype during the experimental campaign can be found in note S12.

The temperature of the first-stage evaporator and last-stage condenser is measured to estimate the temperature drop across the cooler prototype. For this, four 100-ohm PRTs (IEC 60751 tolerance class AA, TC Direct) are used, and their signal is acquired by a dedicated data acquisition system, DAQ (PicoLog PT104, Pico). These 100-ohm PRTs are glued to the aluminum plates in contact with the first-stage evaporator and last-stage condenser. A DC amperemeter (34401A, Agilent) is adopted to measure the electric current flowing through the heaters and, thus, the thermal power supplied to the first-stage evaporator. The distilled water consumed by the evaporators is assessed through a precision scale (PS1000 R2, Radwag). A digital refractometer (HI96801, Hanna Instruments) is used to monitor the salinity of the salt water and distilled water basins and to check for possible contamination of evaporators at the end of each test.

Experimental protocol

Different thermal loads are applied to the cooler prototype through the silicone heaters to explore its characteristic operating curve ($q - \Delta T$). Because the polystyrene envelope does not guarantee perfect insulation from the external environment, heat loss was estimated to correctly evaluate the specific heat flux removed by the cooler (q). The thermal conductance (G) of the polystyrene envelope can be computed using eq. S11, after providing a constant heat flux from the silicone heaters, then measuring the resulting temperature difference by means of the PRTs. Four independent tests were performed, and the obtained average value is $G = (8.5 \pm 0.6) \times 10^{-2}$ W K^{-1} (see note S2 for details). Therefore, the actual specific thermal power removed by the cooler in each test can be calculated as

$$q = \frac{Q + Q_L}{A_{net}} \tag{1}$$

where $Q = VI$, I, and V are the electric current and voltage supplied to the heaters; $Q_L = G(T_A - T_B)$ is the thermal loss; T_A is the temperature of environment where the cooler operates; T_B is the average temperature of the first-stage evaporator; and A_{net} is the effective thermal area of the passive cooling device.

During tests, the temperature difference across the cooler prototype (ΔT) is measured by four PRTs. One is placed in the center of the last-stage condenser, and the remaining three are attached in different positions on the first-stage evaporator (the center of the aluminum plate, and the closest and farthest points from the heaters; see fig. S1) to allow an estimation of temperature uniformity and the associated temperature uncertainty of the tests (see note S2 for details).

The specific flow rate of distilled water (J, m^3 s^{-1} m^{-2}) consumed by evaporators is assessed as

$$J = \frac{\Delta m}{\rho A_{net} \Delta t} - J_{ev} \tag{2}$$

where Δm is the weight difference of the distilled water basin between the beginning and the end of each test (with Δt duration), ρ is the density of distilled water, and J_{ev} is the specific flow rate of the distilled water evaporated in the environment from the basin and the hydrophilic strips before entering the evaporators, therefore causing it to not provide any useful effect. The latter was measured as $J_{ev} = 0.22$ liters m^{-2} $hour^{-1}$ by monitoring the distillate basin weight over time when the evaporation-condensation processes in the cooler were inhibited by the application of impermeable polyethylene films above the membranes in each cooling stage.

Lumped parameter model: Mass transfer

The driving force of the cooling effect from the proposed passive device is the salinity difference between two aqueous solutions, which induces a water vapor pressure difference across the membrane

$$\Delta p_v = a(Y_E)\, p_v(T_E) - a(Y_C)\, p_v(T_C) \tag{3}$$

where a denotes the water activity in the solutions at given concentration Y and temperature T in the evaporator and condenser (subscripts E and C, respectively), and p_v is the vapor pressure of the pure solvent at given temperature. The vapor pressure can be computed via Antoine's semi-empirical correlation as

$$\log(p_v) = A - \frac{B}{C + T} \tag{4}$$

where A, B, and C are the component-specific constants that, in case of water, are estimated as 8.07, 1730.63, and 233.42, respectively (here, p_v is intended in mmHg and T is in Celsius degrees) (*25*). The activity coefficient of water in a salt water solution can be estimated by Raoult's law for ideal mixtures, which is valid in the assumption of low salt concentrations

$$a \approx \frac{1}{1 + m\, M_{H_2O} N_{ions}} \tag{5}$$

where m is the molality of the solution, M_{H2O} is the molar mass of water (expressed in kg mol^{-1}), and N_{ions} is the number of ions composing the salt assuming complete dissociation. On the one side, the feed solution in the evaporators is distilled water, which is characterized by unitary activity coefficient. On the other side, the water activity in the condensers depends on the considered salt concentration of solution.

The specific mass flow rate (J^*, kg s^{-1} m^{-2}) of water vapor through the membrane is evaluated by Maxwell-Stefan and Dusty-Gas models (*26–28*). The Maxwell-Stefan model considers the gradient in chemical potential and the molecular diffusion (namely, the interaction between gas molecules), while the Dusty-Gas model takes into account the viscous flow and the Knudsen diffusion (namely, the interaction between gas molecules and the porous matrix of membrane).

Downloaded from http://advances.sciencemag.org/ on March 14, 2020

Thus, the mass transfer through the porous membrane (z direction) is modeled as

$$-\frac{x_i}{RT}\frac{d\mu_i}{dz} = \frac{x_i K_v \tau}{\eta_v \epsilon_m D_{iK}}\frac{dP}{dz} + \sum_{\substack{j=1 \\ j\neq i}}^{n}\left(\frac{x_j N_i - x_i N_j}{\frac{P\epsilon_m D_{ij}}{RT\tau}}\right) + \frac{N_i}{\frac{P\epsilon_m D_{iK}}{RT\tau}} \quad (6)$$

where x_i and μ_i are the mole fraction and the chemical potential of species i, R is the gas constant (8.314 J K^{-1} mol^{-1}), and T is the absolute temperature. The three terms on the right-hand side of Eq. 6 represent the viscous, molecular, and Knudsen diffusion, respectively. K_v is the viscous permeability coefficient, τ is the tortuosity of the membrane, η_v is the dynamic viscosity of the mixture, ϵ_m is the porosity of the membrane, P is the total pressure of the mixture, and D_{iK} is the Knudsen diffusion coefficient for species i. Then, N_i is the specific molar flux of species i and D_{ij} is the diffusion coefficient of species i in species j. Tortuosity and porosity of membrane can be correlated according to the relation described by Mackie and Meares (*29*, *30*)

$$\tau = \frac{(2-\epsilon_m)^2}{\epsilon_m} \quad (7)$$

Here, the same assumptions discussed by Deshmukh and co-workers (*26*, *27*) and Chiavazzo and co-workers (*19*) are considered to compute J^* from Eq. 6. First, due to the absence of total pressure gradient across the membrane, the viscous term is negligible; therefore, Eq. 6 can be simplified as

$$-\frac{x_w}{RT}\frac{d\mu_w}{dz} = \frac{x_a N_w}{\frac{P\epsilon_m D_{wa}}{RT\tau}} + \frac{N_w}{\frac{P\epsilon_m D_{wK}}{RT\tau}} \quad (8)$$

where x_a and x_w are respectively the mole fractions of air and water vapor ($x_a = 1 - x_w$), N_w is the specific molar flux of water vapor, D_{wa} is the diffusion coefficient of water vapor in air, and D_{wK} is the Knudsen diffusion coefficient of water vapor. In addition, due to the ideal gas assumption, the chemical potential of water vapor (μ_w) is given by $\mu_w = \mu_{w,\,pure} + RT\ln(x_w)$, where the subscripts w and w, pure refer to water and pure water vapor, respectively. The resulting equation is

$$-\frac{dx_w}{dz} = \frac{(1-x_w)N_w}{\frac{P\epsilon_m D_{wa}}{RT\tau}} + \frac{N_w}{\frac{P\epsilon_m D_{wK}}{RT\tau}} \quad (9)$$

Equation 9 can be used to study the water vapor transport through the membrane considering the following boundary conditions: $x_w = x_w^E = \frac{a(Y_E)p_v(T_E)}{P}$ when $z = z_E$ (evaporator side), and $x_w = x_w^C = \frac{a(Y_C)p_v(T_C)}{P}$ when $z = z_C$ (condenser side). The integration of Eq. 9 with these boundary conditions leads to the following expression for the specific mass flow rate of the distillate ($J^* = M_{H_2O}N_w$) through the stage

$$J^* = C_1 \ln\left(\frac{1 + \frac{D_{wa}}{D_{wK}} - x_w^C}{1 + \frac{D_{wa}}{D_{wK}} - x_w^E}\right) \quad (10)$$

where $C_1 = \frac{M_{H_2O}P\epsilon_m D_{wa}}{RT\tau d_m}$ and $d_m = z_C - z_E$ is the membrane thickness. Note that it is possible to empirically estimate $PD_{wa} = 1.19 \times 10^{-4}\,T^{1.75}$ (expressed as Pa m^2 s^{-1}) (*31*) and that the Knudsen diffusion coefficient is defined as

$$D_{wK} = \frac{8r}{3}\sqrt{\left(\frac{RT}{2\pi M_{H_2O}}\right)} \quad (11)$$

where r is the average pore radius of the membrane.

It is worth to point out that, if $x_w \ll 1$, Eq. 10 can be linearly approximated by a first-order Taylor series, namely

$$J^* \approx K\Delta p_v \quad (12)$$

where K is the permeability coefficient of the membrane (*32*). Because the membrane used in the cooler prototype has an average pore size equal to 1.0 μm, transition flow dominates, and the permeability coefficient reported in Eq. 12 can be approximated as

$$\frac{1}{K} = \frac{1}{\frac{\epsilon_m P D_{wa} M_{H_2O}}{p_a \tau RT d_m}} + \frac{1}{\frac{2M_{H_2O}\epsilon_m r}{3RTd_m\tau}\sqrt{\frac{8RT}{\pi M_{H_2O}}}} \quad (13)$$

where p_a is an arithmetic average within the considered domain. In Eq. 13, the membrane permeability is corrected by the p_a/P factor to recover the more general predictions of the Maxwell-Stefan and Dusty-Gas model (*19*). This correction has been successfully applied to numerous membrane distillation experiments in the literature (*33*, *34*). The estimates of the membrane permeability by Eq. 13 are in good agreement with those measured experimentally (see fig. S5).

Considering a possible configuration where an air gap of porosity ϵ_a and thickness d_a is located in series to the membrane, Eq. 9 can be integrated within the air gap and the membrane considering as boundary conditions: $x_w^E = \frac{a(Y_E)p_v(T_E)}{P}$ when $z = z_E$ (evaporator side); $x_w^0 = \frac{a(Y_0)p_v(T_0)}{P}$ when $z = z_0$ (interface between air gap and membrane); $x_w^C = \frac{a(Y_C)p_v(T_C)}{P}$ when $z = z_C$ (condenser side). Clearly, $z_0 - z_E = d_a$ and $z_C - z_0 = d_m$. This integration yields

$$J^* = \frac{C_1}{C_2}\ln\left(\frac{1 - \frac{a(Y_0)p_v(T_0)}{P}}{1 - \frac{a(Y_E)p_v(T_E)}{P}}\right) \quad (14)$$

$$J^* = C_1 \ln\left(\frac{1 + \frac{D_{wa}}{D_{wK}} - \frac{a(Y_C)p_v(T_C)}{P}}{1 + \frac{D_{wa}}{D_{wK}} - \frac{a(Y_0)p_v(T_0)}{P}}\right) \quad (15)$$

where $C_2 = \frac{\epsilon_m d_a}{\tau\epsilon_a d_m}$. Considering the same assumptions and procedure extensively discussed in (*19*), Eqs. 14 and 15 can be combined and the following formulation can be used for evaluating the mass flow rate of the distillate through the stage

$$J^* = C_1 \ln\left[\frac{1 + \frac{D_{wa}}{D_{wK}} - \frac{a(Y_C)p_v(T_C)}{P}}{1 + \frac{D_{wa}}{D_{wK}} - \frac{a(Y_E)p_v(T_E)}{P} + \frac{C_2/C_1}{1/(KP)}\left(\frac{a(Y_E)p_v(T_E)}{P} - \frac{a(Y_C)p_v(T_C)}{P}\right)}\right] \quad (16)$$

where

$$\frac{1}{K} = \frac{1}{\frac{\epsilon_m P D_{wa} M_{H_2O}}{P_a \tau RT d_m}} + \frac{1}{\frac{2M_{H_2O}\epsilon_m r}{3RTd_m\tau}\sqrt{\frac{8RT}{\pi M_{H_2O}}}} + \frac{1}{\frac{\epsilon_a P D_{wa} M_{H_2O}}{P_a RT d_a}} \quad (17)$$

Lumped parameter model: Heat transfer

The specific heat flux (q, W m^{-2}) flowing from the evaporator (hydrophilic layer) to the condenser (salt water cavity) through the membrane (z direction) is mainly due to convective and conductive components, namely (*27*)

$$q = J^*\Delta h_v(Y,T) - \lambda_{eff}\frac{dT}{dz} \quad (18)$$

Downloaded from http://advances.sciencemag.org/ on March 14, 2020

where $\lambda_{eff} = (1 - \epsilon_m)\lambda_p + \epsilon_m\lambda_a$ is the effective thermal conductivity of membrane (λ_p = 0.25 W m^{-1} K^{-1} refers to the polymeric matrix; λ_a = 0.026 W m^{-1} K^{-1} to air) and Δh_v is the enthalpy of vaporization of water, which depends on the salinity (Y) and temperature (T) of the solution. In detail, both the contribution of sensible heat and enthalpy of evaporation should be considered for calculating Δh_v, that is

$$\Delta h_v(Y,T) = c_{p,l}(T_r - T) + \Delta h_v(Y_r,T_r) - c_{p,v}(T_r - T) = \Delta h_v(Y_r,T_r) - \Delta c_p(T - T_r) \quad (19)$$

where $c_{p,l}$ and $c_{p,v}$ are the isobaric-specific heat capacities of the liquid and vapor phase of water, respectively, and $\Delta c_p = c_{p,l} - c_{p,v}$ (*27*). In Eq. 19, liquid water is supposed to increase its temperature from T to T_r (reference temperature), then to evaporate at T_r (considering a reference salinity Y_r), and finally water vapor to cool down from T_r back to the initial T. By including Eq. 19 into Eq. 18, we obtain

$$q = J^*\left[\Delta h_v(Y_r,T_r) - \Delta c_p(T - T_r)\right] - \lambda_{eff}\frac{dT}{dz} \quad (20)$$

Equation 20 can be integrated within the membrane considering $T = T_E$ at $z = z_E$ (evaporator side) and $T = T_C$ at $z = z_C$ (condenser side) as boundary conditions, which yields

$$\int_{T=T_E}^{T=T_C}\left[T - T_r + \frac{1}{\Delta c_p}\left(\frac{q}{J^*} - \Delta h_v(Y_r,T_r)\right)\right]^{-1} dT = -\frac{J^*\Delta c_p d_m}{\lambda_{eff}} \quad (21)$$

Here, $T_r = T_E$, $Y_r = Y_E$ are set as reference conditions for convenience, therefore leading to

$$q = J^*\Delta h_v(Y_E,T_E) + \frac{J^*\Delta c_p(T_C - T_E)}{\exp\left(-\frac{J^*\Delta c_p d_m}{\lambda_{eff}}\right) - 1} \quad (22)$$

Because $\frac{J^*\Delta c_p d_m}{\lambda_{eff}} \ll 1$, the first-order Taylor approximation of Eq. 22 becomes

$$q \approx J^*\Delta h_v(Y_E,T_E) - \frac{\lambda_{eff}}{d_m}(T_C - T_E) \quad (23)$$

An equivalent thermal resistance circuit that schematically represents this 1D model approximation is presented in fig. S12. Note that the thermal resistance associated with the salt water cavity (i.e., the condenser) in each stage is estimated assuming natural convection. To this purpose, the Nusselt-Rayleigh correlation has been adopted (*35*), where the Nusselt number is estimated as Nu ≈ 1 (*35*) and the Rayleigh number is computed as

$$\mathrm{Ra} = \frac{g\beta h^3(T_E - T_C)}{\alpha\nu} \quad (24)$$

where g is the standard acceleration due to gravity, β is the thermal expansion coefficient of water (207×10^{-6} K^{-1} at ambient temperature), h is the thickness of salt water cavity (≈2 mm), α is the thermal diffusivity of water (0.143×10^{-6} m^2 s^{-1}), and ν is the kinematic viscosity of water (10^{-6} m^2 s^{-1}).

An illustrative 1D temperature profile throughout the cooling stages in case of a 1-, 4-, and 10-stage configuration device is depicted in fig. S13. The 1D approximation of heat transfer adopted in the model above has been demonstrated to be an accurate one, because boundary effects do not substantially alter the homogeneous temperature distributions in each stage (see note S13 and fig. S14).

Statistical analysis

See note S2 for details on the reported error bars as well as statistical and uncertainty analyses of experimental measurements.

SUPPLEMENTARY MATERIALS

Supplementary material for this article is available at http://advances.sciencemag.org/cgi/content/full/6/11/eaax5015/DC1

Note S1. Membrane permeability measurement
Note S2. Measurement uncertainty analysis
Note S3. Solute transport through the condensing side
Note S4. Exergy analysis of the passive cooler
Note S5. Comparison with other passive cooling approaches
Note S6. Details on the coupling between passive distiller and cooler
Note S7. Coefficient of performance
Note S8. Coupling with high-salinity brines produced by different desalination technologies
Note S9. Cost analysis of the laboratory-scale prototypes
Note S10. Considerations on environmental and life-cycle analysis issues of the passive cooler
Note S11. Cooling performance of the device under the sun
Note S12. Durability and corrosion of the passive cooler
Note S13. Boundary effects on the temperature field in the evaporator
Fig. S1. Experimental setup to measure cooling capacity.
Fig. S2. Assembly of the passive cooling device.
Fig. S3. Natural mass transport phenomena in the present passive cooler.
Fig. S4. Distillate consumption by the passive cooler.
Fig. S5. Experimental results and modeling predictions of membrane permeability.
Fig. S6. Possible spacer for enhancing the cooler performance.
Fig. S7. Distillate consumption by the passive cooler for different air gaps.
Fig. S8. Qualitative thermodynamic cycle of a passive solar cooling cycle.
Fig. S9. Coupling between the passive cooler and distiller to implement a stable cooling cycle.
Fig. S10. Mirror screening of the cooler exposed to the sun.
Fig. S11. SIMSCAPE implementation of the mirror screening of the cooler exposed to the sun.
Fig. S12. Lumped model for the heat transfer in the passive cooler.
Fig. S13. Temperature profiles across the cooling stages in case of a 1-, 4-, and 10-stage configuration device.
Fig. S14. Results of the finite element model for the hydrophilic layer (evaporator).
Fig. S15. Passive cooler operating with high-salinity brines produced by different desalination technologies.
Table S1. Uncertainties in the theoretical model.
Table S2. Exergy performance of the passive cooler with different number of stages.
Table S3. Estimated costs for the prototype of passive cooler.
Table S4. Estimated costs for the prototype of passive distiller considered here to implement a solar cooling cycle.
Table S5. Parameters considered for the simulations of the cooler performance under the sun.
Dataset S1. Experimental raw data of tests with NaCl.
Dataset S2. Experimental raw data of tests with $CaCl_2$.
References (*41*–*75*)

REFERENCES AND NOTES

1. D. Ürge-Vorsatz, L. F. Cabeza, S. Serrano, C. Barreneche, K. Petrichenko, Heating and cooling energy trends and drivers in buildings. *Renew. Sustain. Energy Rev.* **41**, 85–98 (2015).
2. M. Jakubcionis, J. Carlsson, Estimation of european union residential sector space cooling potential. *Energy Policy* **101**, 225–235 (2017).
3. D. H. Li, L. Yang, J. C. Lam, Impact of climate change on energy use in the built environment in different climate zones—A review. *Energy* **42**, 103–112 (2012).
4. S. Bhattacharya, "The 2003 European heatwave caused 35,000 deaths," *New Scientist*, 10 October 2003.
5. International Energy Agency, *The Future of Cooling: Opportunities for Energy Efficient Air Conditioning* (OECD/IEA, 2018).
6. M. Mohanraj, S. Jayaraj, C. Muraleedharan, Environment friendly alternatives to halogenated refrigerants—A review. *Int. J. Greenh. Gas. Control* **3**, 108–119 (2009).

Downloaded from http://advances.sciencemag.org/ on March 14, 2020

7. M. H. Mahmood, M. Sultan, T. Miyazaki, S. Koyama, V. S. Maisotsenko, Overview of the Maisotsenko cycle–A way towards dew point evaporative cooling. *Renew. Sustain. Energy Rev.* **66**, 537–555 (2016).
8. C. Wani, S. Ghodke, C. Shrivastava, A review on potential of Maisotsenko cycle in energy saving applications using evaporative cooling. *Int. J. Adv. Res. Sci. Eng. Technol.* **1**, 15–20 (2012).
9. M. Zeyghami, D. Y. Goswami, E. Stefanakos, A review of clear sky radiative cooling developments and applications in renewable power systems and passive building cooling. *Sol. Energ. Mat. Sol. C.* **178**, 115–128 (2018).
10. A. P. Raman, M. A. Anoma, L. Zhu, E. Rephaeli, S. Fan, Passive radiative cooling below ambient air temperature under direct sunlight. *Nature* **515**, 540–544 (2014).
11. Y. Zhai, Y. Ma, S. N. David, D. Zhao, R. Lou, G. Tan, R. Yang, X. Yin, Scalable-manufactured randomized glass-polymer hybrid metamaterial for daytime radiative cooling. *Science* **355**, 1062–1066 (2017).
12. J. Mandal, Y. Fu, A. C. Overvig, M. Jia, K. Sun, N. N. Shi, H. Zhou, X. Xiao, N. Yu, Y. Yang, Hierarchically porous polymer coatings for highly efficient passive daytime radiative cooling. *Science* **362**, 315–319 (2018).
13. S. Buddhiraju, P. Santhanam, S. Fan, Thermodynamic limits of energy harvesting from outgoing thermal radiation. *Proc. Natl. Acad. Sci. U.S.A.* **115**, E3609–E3615 (2018).
14. E. A. Goldstein, A. P. Raman, S. Fan, Sub-ambient non-evaporative fluid cooling with the sky. *Nat. Energy* **2**, 17143 (2017).
15. J. K. Tong, X. Huang, S. V. Boriskina, J. Loomis, Y. Xu, G. Chen, Infrared-transparent visible-opaque fabrics for wearable personal thermal management. *ACS Photonics* **2**, 769–778 (2015).
16. C. Granqvist, A. Hjortsberg, Radiative cooling to low temperatures: General considerations and application to selectively emitting SiO films. *J. Appl. Phys.* **52**, 4205–4220 (1981).
17. A. K. Head, Method and means for refrigeration by selective radiation. Australian Patent 239364 (1959).
18. J. Woods, J. Pellegrino, E. Kozubal, S. Slayzak, J. Burch, Modeling of a membrane-based absorption heat pump. *J. Membr. Sci.* **337**, 113–124 (2009).
19. E. Chiavazzo, M. Morciano, F. Viglino, M. Fasano, P. Asinari, Passive solar high-yield seawater desalination by modular and low-cost distillation. *Nat. Sustain.* **1**, 763–772 (2018).
20. R. D. M. Rocha, D. F. Costa, M. A. Lucena-Filho, R. M. Bezerra, D. H. Medeiros, A. M. Azevedo-Silva, C. N. Araújo, L. Xavier-Filho, Brazilian solar saltworks-ancient uses and future possibilities. *Aquat. Biosyst.* **8**, 8 (2012).
21. P. Wang, Emerging investigator series: The rise of nano-enabled photothermal materials for water evaporation and clean water production by sunlight. *Environ. Sci. Nano* **5**, 1078–1089 (2018).
22. H. Aral, A. Vecchio-Sadus, Toxicity of lithium to humans and the environment—A literature review. *Ecotoxicol. Environ. Saf.* **70**, 349–356 (2008).
23. D. J. Randall, T. Tsui, Ammonia toxicity in fish. *Mar. Pollut. Bull.* **45**, 17–23 (2002).
24. M. Morciano, M. Fasano, U. Salomov, L. Ventola, E. Chiavazzo, P. Asinari, Efficient steam generation by inexpensive narrow gap evaporation device for solar applications. *Sci. Rep.* **7**, 11970 (2017).
25. B. E. Poling, J. M. Prausnitz, J. P. O'connell, *The Properties of Gases and Liquids* (McGraw-Hill, 2001), vol. 5.
26. A. Deshmukh, C. Boo, V. Karanikola, S. Lin, A. P. Straub, T. Tong, D. M. Warsinger, M. Elimelech, Membrane distillation at the water-energy nexus: Limits, opportunities, and challenges. *Energ. Environ. Sci.* **11**, 1177–1196 (2018).
27. A. Deshmukh, M. Elimelech, Understanding the impact of membrane properties and transport phenomena on the energetic performance of membrane distillation desalination. *J. Membr. Sci.* **539**, 458–474 (2017).
28. J. Lee, A. P. Straub, M. Elimelech, Vapor-gap membranes for highly selective osmotically driven desalination. *J. Membr. Sci.* **555**, 407–417 (2018).
29. J. Mackie, P. Meares, The diffusion of electrolytes in a cation-exchange resin membrane I. Theoretical. *Proc. R. Soc. Lond. A* **232**, 498–509 (1955).
30. S. Srisurichan, R. Jiraratananon, A. Fane, Mass transfer mechanisms and transport resistances in direct contact membrane distillation process. *J. Membr. Sci.* **277**, 186–194 (2006).
31. Y. Yun, R. Ma, W. Zhang, A. Fane, J. Li, Direct contact membrane distillation mechanism for high concentration NaCl solutions. *Desalination* **188**, 251–262 (2006).
32. J.-G. Lee, Y.-D. Kim, W.-S. Kim, L. Francis, G. Amy, N. Ghaffour, Performance modeling of direct contact membrane distillation (DCMD) seawater desalination process using a commercial composite membrane. *J. Membr. Sci.* **478**, 85–95 (2015).
33. K. W. Lawson, D. R. Lloyd, Membrane distillation. *J. Membr. Sci.* **124**, 1–25 (1997).
34. R. W. Schofield, A. G. Fane, C. J. D. Fell, R. Macoun, Factors affecting flux in membrane distillation. *Desalination* **77**, 279–294 (1990).
35. E. Abu-Nada, H. F. Oztop, Effects of inclination angle on natural convection in enclosures filled with Cu–water nanofluid. *Int. J. Heat Fluid Flow* **30**, 669–678 (2009).
36. E. Rephaeli, A. Raman, S. Fan, Ultrabroadband photonic structures to achieve high-performance daytime radiative cooling. *Nano Lett.* **13**, 1457–1461 (2013).
37. M. A. Kecebas, M. P. Menguc, A. Kosar, K. Sendur, Passive radiative cooling design with broadband optical thin-film filters. *J. Quant. Spectrosc. Radiat.* **198**, 179–186 (2017).
38. Y. Fu, J. Yang, Y. Su, W. Du, Y. Ma, Daytime passive radiative cooler using porous alumina. *Sol. Energy Mater. Sol. Cells* **191**, 50–54 (2019).
39. T. M. Nilsson, G. A. Niklasson, C.-G. Granqvist, in *Optical Materials Technology for Energy Efficiency and Solar Energy Conversion XI: Selective Materials, Concentrators and Reflectors, Transparent Insulation and Superwindows* (International Society for Optics and Photonics, 1992), vol. 1727, pp. 249–262.
40. B. Bhatia, A. Leroy, Y. Shen, L. Zhao, M. Gianello, D. Li, T. Gu, J. Hu, M. Soljačić, E. N. Wang, Passive directional sub-ambient daytime radiative cooling. *Nat. Commun.* **9**, 5001 (2018).
41. S. Globe, D. Dropkin, Natural-convection heat transfer in liquids confined by two horizontal plates and heated from below. *J. Heat Transfer* **81**, 24–28 (1959).
42. C. J. Geankoplis, *Transport Processes and Separation Process Principles (Includes Unit Operations)* (Prentice Hall Professional Technical Reference, ed. 4, 2003).
43. K. G. Nayar, M. H. Sharqawy, J. H. Lienhard V, Seawater thermophysical properties library (2016); http://web.mit.edu/seawater/2017_MIT_Seawater_Property_Tables_r2a.pdf [accessed 16 October 2019].
44. D. Winter, *Membrane Distillation. A Thermodynamic, Technological and Economic Analysis* (Shaker Verlag, 2015).
45. H. Kitahata, N. Yoshinaga, Effective diffusion coefficient including the marangoni effect. *J. Chem. Phys.* **148**, 134906 (2018).
46. M. Morciano, "Solar energy technologies for passive and low-cost water desalination," thesis, Politecnico di Torino, Torino (2019).
47. N. A. Vinnichenko, A. V. Uvarov, D. A. Vetukov, Y. Y. Plaksina, Recent researches in mechanics, in *Proceedings of the 2nd International Conference on FLUIDSHEAT'11* (WSEAS Press, 2011).
48. Y. A. Cengel, S. Klein, W. Beckman, *Heat Transfer: A Practical Approach* (McGraw-Hill, 1998), vol. 141.
49. T. Suichi, A. Ishikawa, Y. Hayashi, K. Tsuruta, Performance limit of daytime radiative cooling in warm humid environment. *AIP Adv.* **8**, 055124 (2018).
50. G. G. Amenu, P. Kumar, NVAP and reanalysis-2 global precipitable water products: Intercomparison and variability studies. *Bull. Am. Meteorol. Soc.* **86**, 245–256 (2005).
51. M. Rosen, A. Bejan, *Thermal Energy Storage Systems and Applications* (John Wiley & Sons, 2002).
52. J. H. Lienhard, G. P. Thiel, D. M. Warsinger, L. D. Banchik, *Low Carbon Desalination: Status and Research, Development, and Demonstration Needs, Report of a Workshop Conducted at the Massachusetts Institute of Technology in Association with the Global Clean Water Desalination Alliance* (Massachusetts Institute of Technology, 2016).
53. I. Sarbu, C. Sebarchievici, Review of solar refrigeration and cooling systems. *Energ. Buildings* **67**, 286–297 (2013).
54. A. Ghafoor, A. Munir, Worldwide overview of solar thermal cooling technologies. *Renew. Sustain. Energy Rev.* **43**, 763–774 (2015).
55. E. Jones, M. Qadir, M. T. H. van Vliet, V. Smakhtin, S.-M. Kang, The state of desalination and brine production: A global outlook. *Sci. Total Environ.* **657**, 1343–1356 (2018).
56. A. Demirbas, A. A. Hashem, A. A. Bakhsh, The cost analysis of electric power generation in saudi arabia. *Energ. Source. Part B* **12**, 591–596 (2017).
57. T. Tong, M. Elimelech, The global rise of zero liquid discharge for wastewater management: Drivers, technologies, and future directions. *Environ. Sci. Technol.* **50**, 6846–6855 (2016).
58. R. L. McGinnis, N. T. Hancock, M. S. Nowosielski-Slepowron, G. D. McGurgan, Pilot demonstration of the NH_3/CO_2 forward osmosis desalination process on high salinity brines. *Desalination* **312**, 67–74 (2013).
59. J. Morillo, J. Usero, D. Rosado, H. El Bakouri, A. Riaza, F.-J. Bernaola, Comparative study of brine management technologies for desalination plants. *Desalination* **336**, 32–49 (2014).
60. H. W. Chung, J. Swaminathan, D. M. Warsinger, J. H. Lienhard V, Multistage vacuum membrane distillation (MSVMD) systems for high salinity applications. *J. Membr. Sci.* **497**, 128–141 (2016).
61. M. Safavi, T. Mohammadi, High-salinity water desalination using VMD. *Chem. Eng. J.* **149**, 191–195 (2009).
62. U.S. Environmental Protection Agency, *Advancing Sustainable Materials Management: Facts and Figures Report* (U.S. Environmental Protection Agency, 2018).
63. M. d. G. T. García, M. Schlatter, F. M. Cabrera, J. T. Manzanares, I. Hanafi, Recycling of acrylonitrile–butadiene–styrene using injection moulding machine. *Proc. Tech.* **22**, 399–406 (2016).
64. A. Lakshmanan, S. Chakraborty, in *Sintering Techniques of Materials* (IntechOpen, 2015).
65. C. Cao, L. Liu, Q. Li, P. Chen, Q. Qian, Q. Chen, Recycling and application of wasted polytetrafluoroethylene via high-energy ball milling technology for nitrile rubber composites preparation. *Polym. Eng. Sci.* **56**, 643–649 (2016).

Downloaded from http://advances.sciencemag.org/ on March 14, 2020

66. M. A. Browne, P. Crump, S. J. Niven, E. Teuten, A. Tonkin, T. Galloway, R. Thompson, Accumulation of microplastic on shorelines woldwide: Sources and sinks. *Environ. Sci. Technol.* **45**, 9175–9179 (2011).
67. S. Lattemann, T. Höpner, Environmental impact and impact assessment of seawater desalination. *Desalination* **220**, 1–15 (2008).
68. R. Einav, K. Harussi, D. Perry, The footprint of the desalination processes on the environment. *Desalination* **152**, 141–154 (2003).
69. J. L. Sánchez-Lizaso, J. Romero, J. Ruiz, E. Gacia, J. L. Buceta, O. Invers, Y. F. Torquemada, J. Mas, A. Ruiz-Mateo, M. Manzanera, Salinity tolerance of the Mediterranean seagrass *Posidonia oceanica*: Recommendations to minimize the impact of brine discharges from desalination plants. *Desalination* **221**, 602–607 (2008).
70. M. H. El-Naas, *Desalination, Trends and Technologies* (IntechOpen, 2011).
71. A. M. O. Mohamed, M. Maraqa, J. Al Handhaly, Impact of land disposal of reject brine from desalination plants on soil and groundwater. *Desalination* **182**, 411–433 (2005).
72. O. Abessi, *Sustainable Desalination Handbook* (Elsevier, 2018), pp. 259–303.
73. L. Ventola, F. Robotti, M. Dialameh, F. Calignano, D. Manfredi, E. Chiavazzo, P. Asinari, Rough surfaces with enhanced heat transfer for electronics cooling by direct metal laser sintering. *Int. J. Heat Mass Transfer* **75**, 58–74 (2014).
74. S. Adnan, M. Hoang, H. Wang, Z. Xie, Commercial PTFE membranes for membrane distillation application: Effect of microstructure and support material. *Desalination* **284**, 297–308 (2012).
75. M. M. A. Shirazi, A. Kargari, M. Tabatabaei, Evaluation of commercial PTFE membranes in desalination by direct contact membrane distillation. *Chem. Eng. Process.* **76**, 16–25 (2014).

Acknowledgments: We thank M. Bressan and R. Costantino for laboratory support. We also thank C. Iazzetta, A. Fieno, and X. Xenofon for preliminary experiments. **Funding:** We are grateful to the NANOSTEP (La Ricerca dei Talenti, Fondazione CRT—Torino, grant number: 911/2015) project. E.C. acknowledges partial financial support by Politecnico di Torino (starting grant no. 56_RIL16CHE01 and grant no. 56_RBA17CHI01). **Author contributions:** E.C. conceived the idea of this study and, together with P.A., supervised research activities. P.A. initially suggested the use of hydrophobic microporous membranes for seawater desalination and developed the theoretical model. M.A. and M.M. engineered the prototype and conducted all experiments and simulations. F.B. and V.F. helped with the metrological aspects of the experiments. M.F. helped with the prototype assembly, testing, and supervision. M.A., M.M., M.F., P.A., and E.C. analyzed the results and wrote the paper. **Competing interests:** The authors declare that they have no competing interests. **Data and materials availability:** All data needed to evaluate the conclusions in the paper are present in the paper and/or the Supplementary Materials. Additional data related to this paper may be requested from the authors.

Submitted 28 March 2019
Accepted 16 December 2019
Published 13 March 2020
10.1126/sciadv.aax5015

Citation: M. Alberghini, M. Morciano, M. Fasano, F. Bertiglia, V. Fernicola, P. Asinari, E. Chiavazzo, Multistage and passive cooling process driven by salinity difference. *Sci. Adv.* **6**, eaax5015 (2020).

Downloaded from http://advances.sciencemag.org/ on March 14, 2020

Science Advances

Multistage and passive cooling process driven by salinity difference

Matteo Alberghini, Matteo Morciano, Matteo Fasano, Fabio Bertiglia, Vito Fernicola, Pietro Asinari and Eliodoro Chiavazzo

Sci Adv **6** (11), eaax5015.
DOI: 10.1126/sciadv.aax5015

ARTICLE TOOLS http://advances.sciencemag.org/content/6/11/eaax5015

SUPPLEMENTARY MATERIALS http://advances.sciencemag.org/content/suppl/2020/03/09/6.11.eaax5015.DC1

REFERENCES This article cites 58 articles, 3 of which you can access for free
http://advances.sciencemag.org/content/6/11/eaax5015#BIBL

PERMISSIONS http://www.sciencemag.org/help/reprints-and-permissions

Use of this article is subject to the Terms of Service

Science Advances (ISSN 2375-2548) is published by the American Association for the Advancement of Science, 1200 New York Avenue NW, Washington, DC 20005. The title *Science Advances* is a registered trademark of AAAS.

Copyright © 2020 The Authors, some rights reserved; exclusive licensee American Association for the Advancement of Science. No claim to original U.S. Government Works. Distributed under a Creative Commons Attribution NonCommercial License 4.0 (CC BY-NC).

Downloaded from http://advances.sciencemag.org/ on March 14, 2020